Eur. Phys. J. B **48**, 359–365 (2005)
DOI: 10.1140/epjb/e2005-00413-y

THE EUROPEAN PHYSICAL JOURNAL B

Intrinsic pinning and current percolation signatures in E-J characteristics of Si/YSZ/CeO_2/YBCO layouts

D. Botta[1], C. Camerlingo[2], A. Chiodoni[1], F. Fabbri[3], R. Gerbaldo[1], G. Ghigo[1], L. Gozzelino[1], F. Laviano[1], B. Minetti[1], C.F. Pirri[1], G. Rombolà[1], G. Tallarida[4], E. Tresso[1], and E. Mezzetti[1,a]

[1] Dipartimento di Fisica, Politecnico di Torino, c.^{so} Duca degli Abruzzi 24, 10129 Torino, Italy
[2] Consiglio Nazionale delle Ricerche, Istituto di Cibernetica "E. Caianiello", via Campi Flegrei 34, 80078 Pozzuoli (Na), Italy
[3] Enea-Frascati, via Enrico Fermi, 45, 00044 - Frascati, Roma, Italy
[4] INFM - Laboratorio MDM, via Olivetti 2, 20041 Agrate Brianza (Mi), Italy

Received 22 July 2005 / Received in final form 26 October 2005
Published online 23 December 2005 –

Abstract. In the context of superconducting electronics integrated with traditional silicon-based electronics we grew Si/YSZ/CeO_2/$YBa_2Cu_3O_{7-x}$ architectures by means of the scalable magnetron sputtering growth technique. In this paper we report on structural, surface and electrical transport characterization of typical multilayers. We focus on the electrical transport characterization in the temperature range 18–30 K of *c*-axis $YBa_2Cu_3O_{7-x}$ films grown on top of several (001) oriented buffered substrates. The electric field vs. current density (*E*-*J*) curves exhibit step-like behaviour in correspondence to the transition between the non-dissipative and the flux-flow regimes. This trend is accompanied by the signature of linearly correlated pinning. On the other hand, in the flux-flow regime clear signatures of weak-link behaviour and current percolation are exhibited. In this complex framework possible future applications are discussed.

PACS. 74.78.Fk Multilayers, superlattices, heterostructures – 74.25.Fy Transport properties (electric and thermal conductivity, thermoelectric effects, etc.) – 68.55.-a Thin film structure and morphology – 81.15.Cd Deposition by sputtering

1 Introduction

Exploiting the unique properties of superconductors, such as $YBa_2Cu_3O_{7-x}$ (YBCO), in the framework of semiconductor-superconductor integrated electronics, depends on the employment of scalable growth techniques as those available in a semiconductor foundry, where large-area YBCO growth processes can be integrated with conventional semiconductor technology thus creating read-out and bias circuitry on the same chip. YBCO films exhibit optimal band gap, high critical temperature, T_c, and ultra-fast (about 1 ps) voltage photo-response when optically excited with pulsed laser beam [1]. Furthermore, despite what is commonly believed, optimally oxygenated films are robust with respect to aging in a standard environment.

Several authors addressed the matter since the early stage of the superconducting films applications. G. Beddies et al. [2] succeeded in preparing by PLD (Pulsed Laser Deposition) epitaxially grown YSZ (Yttria Stabilized Zirconia) — buffered YBCO on Si substrate, exhibiting critical temperature higher than 88K and critical current density J_c as large as 2×10^{10} A/m^2. Envisaged technological problems, due to the damage related to the chemical etching and to the lack of perspective in submicron lithography, were claimed (at that time focalized ion-beam lithography techniques were not available yet). Recently, Méchin et al. [3] took advantage of a long route of studies on PLD growth of YBCO films on buffered Si substrates [4], to present a co-fabrication of superconducting YBCO and semiconducting p-MOS circuitry, aimed at bolometric applications.

In this framework, the magnetron sputtering growth technique has to be considered in order to establish which are the opportunities to grow large-area robust monolithic YBCO/silicon integrated devices. With respect to specific traditional substrates used for superconductor technology, already-existing low-cost microlithography processing and micromachining technique make the YBCO/silicon integration very appealing for low-power applications.

As it is known, the growth of YBCO films on silicon requires buffer layers to avoid lattice and thermal-expansion coefficient mismatches between YBCO and silicon [4–8]. The most frequently proposed buffer layers in the recent literature are YSZ and CeO_2. YSZ has an optimal matching with (001) oriented silicon and grows (001) oriented as the substrate itself. A thin layer of CeO_2 on YSZ assumes the right orientation (001) as well [4,8,9]. Such buffered substrate allows the growth of *c*-axis oriented YBCO film on top [5,10].

[a] e-mail: enrica.mezzetti@polito.it

Table 1. Experimental growth conditions and some details concerning the electrical transport characterization for two samples E45 and E47 representative of the two kinds of differently grown Si/YSZ/CeO_2/YBCO multilayers presented in this paper.

Sample	YSZ	CeO_2	YBCO	Comments	Voltage contacts distance	Cross-section
E45	$T_{growth} = 730$ °C	$T_{growth} = 730$ °C	$T_{growth} = 733$ °C	YSZ/CeO_2 in-situ growth	0.15 cm	375×10^{-12} m^2
	$P_{Ar} = 0.13$ Pa	$P_{Ar} = 0.13$ Pa	Ar/O_2 (4:3) gas mixture with a total pressure of 93 Pa			
E47	$T_{growth} = 730$ °C	$T_{growth} = 744$ °C	$T_{growth} = 732$ °C	CeO_2/YBCO in-situ growth	0.40 cm	125×10^{-12} m^2
	$P_{Ar} = 0.13$ Pa	Ar/O_2 (1:1) gas mixture with a total pressure of 0.95 Pa	Ar/O_2 (4:3) mixture with a total pressure of 93 Pa			

Moreover the CeO_2 layer guarantees a barrier effect against possible chemical reactions between the YBCO film and the substrate.

In this paper we report on structural and electrical transport characterizations of Si/YSZ/CeO_2/YBCO architectures prepared on 1 cm × 1 cm (001) oriented Si substrates by means of the magnetron sputtering technique. Taking into account that the uniform deposition area is about 5 cm × 5 cm, during each deposition run several twin samples were prepared, each of them aimed at different characterizations. It turns out that in the range of temperatures from 18 to 30 K these *c*-axis oriented YBCO films exhibit a step-like current-voltage characteristics across the transition between the non-dissipative and the flux-flow regimes. This trend is accompanied by the signature of a linearly correlated pinning. In the flux-flow regime clear signatures of weak-link regime and current percolation are also shown. A study of this particular weak-link regime is reported to start exploring the intrinsic potentiality for large-area applications.

2 Growth process and characterization experimental details

Different Si/YSZ/CeO_2/YBCO multilayers were prepared by means of the magnetron sputtering technique. Two different procedures were followed. The first one consists in an in-situ growth of the YSZ/CeO_2 buffer layers on the Si substrate followed by an ex-situ YBCO deposition. The second one consists in the YSZ layer growth on Si, followed by an in-situ deposition of the CeO_2/YBCO bilayer.

The YSZ layer (nominal thickness: 15 nm) was grown as follows: after a degreasing procedure in acetone and ultrasonic ethanol bath, the silicon substrate was chemically etched in a 0.4% HF solution until hydrophobic, in order to remove the native silicon dioxide. Then the substrates were dipped in de-ionized water and blown with N_2. Once loaded into the sample holder, they were heated up to 730 °C under vacuum. As soon as the substrates reached the deposition temperature, Ar at 0.13 Pa was introduced in the sputtering chamber and the plasma was switched on with a RF power of 80 W. Afterwards, CeO_2 and YBCO layers were grown on top of the YSZ film.

The CeO_2 growth was performed by means of a RF magnetron sputtering as follows: in a Ar plasma with forward RF power of 80 W and at temperature of 730 °C, for what concerns the YSZ/CeO_2 in-situ growth (nominal CeO_2 thickness: 30 nm), and in a mixed Ar/O_2 plasma with forward RF power of 55 W (temperature of 744 °C), for what concerns the CeO_2/YBCO in-situ growth (nominal CeO_2 thickness: 10 nm). We optimised the CeO_2 thickness in order to guarantee a barrier against possible chemical reactions between the YBCO film and the substrate and in order to obtain multilayers without aging problems in a standard environment.

The YBCO films (nominal YBCO thickness: 250 nm) were grown by means of the inverted cylindrical DC magnetron sputtering technique at temperature of about 730 °C, in a mixed Ar/O_2 (4:3) plasma and with a power of 100 W. After the deposition, the chamber was filled with 40 kPa of oxygen and the temperature was slowly decreased (5 °C/min) until the substrate temperature $T = 600$ °C was reached. The oxygen pressure was increased to the value of 80 kPa, and the temperature slowly decreased to 450 °C. After a rest of 30 min, the heater was turned off.

The structural properties of each layer were investigated by means of standard θ–2θ X-ray diffraction and non-contact atomic force microscopy (AFM). We studied the role of each layer with respect to the final multilayer properties, in order to correlate the YBCO superconducting performance with its structural characteristics as well as with the buffered substrate properties. The electric transport characterization of the complete multilayer was carried out by means of a standard four-probe technique as a function of temperature and bias current.

All the details concerning the growth procedure of two architectures representative of these two different growth procedures are summarized in Table 1.

3 Structural characterization

3.1 X-ray diffraction characterization

The θ–2θ X-ray diffraction patterns of the E45 and E47 multilayers, representative of the two different growth procedures described in Section 2, are reported in Figure 1.

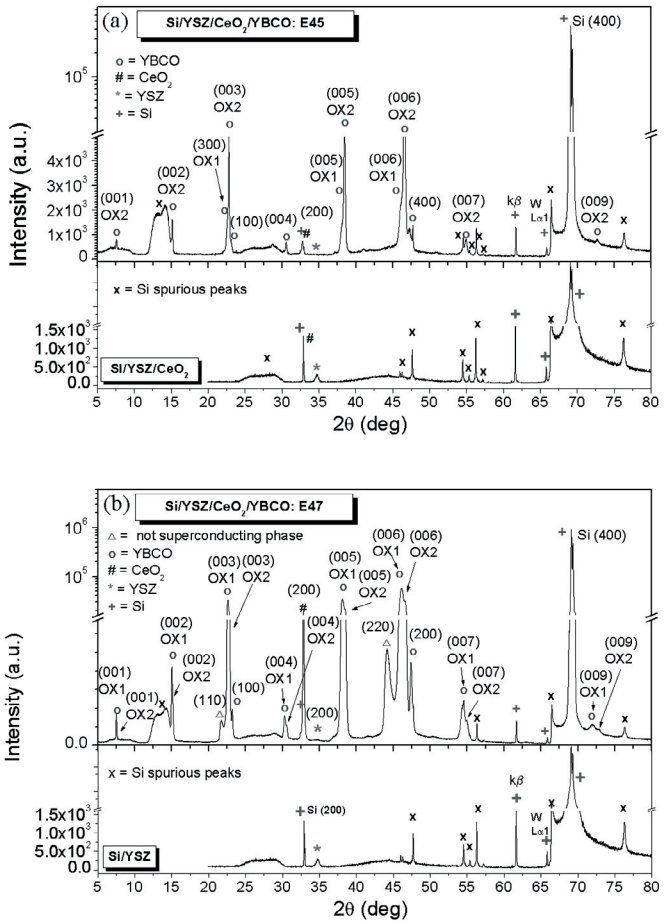

Fig. 1. θ–2θ X-ray diffraction patterns of the two Si/YSZ/CeO2/YBCO samples E45 (a) and E47 (b). The corresponding X-ray diffraction characterization of first growth step of the multilayer is also reported for both the samples.

The X-ray diffraction measurements of the first growth step of the two multilayers are also reported. It results that in both samples the buffer layers are (001) oriented. Moreover, both E45 and E47 samples exhibit a prevalent c-axis orientation, although some slightly intense peaks belonging to the (h00) family can be found. Both samples show a double YBCO oriented phase (OX1, OX2). Sample E47 exhibits also other two peaks at about 21.73° and 44.22°, probably related to a not superconducting phase.

In Table 2, the value of the c-axis for the two samples, as obtained by linearly fitting the c-axis associated to each (00l) peak as a function of the corresponding $\cos\theta \cot\theta$ data [11], is reported. For both samples there are two different c-axis evaluations because of the double phase in the X-ray spectrum.

By considering the c-axis length, also the oxygen content in the $YBa_2Cu_3O_{7-x}$ film was calculated using the empirical equation suggested in reference [12] and is reported in Table 2. The two oxygen contents are attributed to a non superconducting tetragonal phase (OX1) and to a superconducting orthorhombic phase (OX2), respectively. Sample E47 shows a higher oxygen content of the orthorhombic phase that justifies its better superconducting properties with respect to sample E45.

Table 2. Experimental c-axis values and oxygen content of samples E45 and E47.

Sample	*c-axis*	Oxygen content
E45	OX1: 11.799 ± 0.007 Å	6.41
	OX2: 11.697 ± 0.005 Å	6.89
E47	OX1: 11.815 ± 0.004 Å	6.34
	OX2: 11.674 ± 0.007 Å	6.98

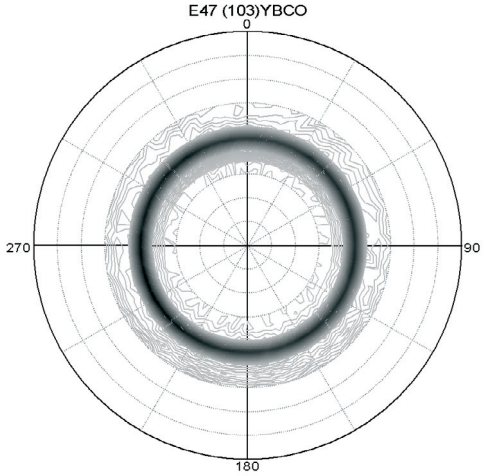

Fig. 2. Texture measurement of sample E47 on the (103) YBCO.

Texture measurements performed either on the buffer layers or on the YBCO films show a fibre texture, i.e., a random in plane orientation (Fig. 2).

3.2 AFM characterization

AFM analysis were performed in order to compare the surface morphology of the films, that is also related to the bulk arrangement of the grain clusters.

A comparison between the surface morphology of the buffered silicon and the YBCO film grown on top, is presented in Figure 3 for both the samples. In Figure 3a, the CeO_2 morphology in the Si/YSZ/CeO_2 multilayer (lower), before the deposition of the YBCO film (upper), is depicted (sample E45). The top buffer layer results to be very flat, with a roughness of about 1 nm. The YBCO film exhibits a roughness of about 73 nm. In Figure 3b the morphology of YSZ in the Si/YSZ bilayer (lower), before the deposition of the CeO_2/YBCO films (upper), is reported (sample E47). Also in this case, the YSZ buffer layer results to be very flat, with a roughness of about 1 nm, while the YBCO film exhibits a roughness of about 88 nm.

A more detailed AFM investigation of both the YBCO films surface morphology is shown in two subsequent enlargements (10 μm × 10 μm and 5μm × 5 μm) reported in

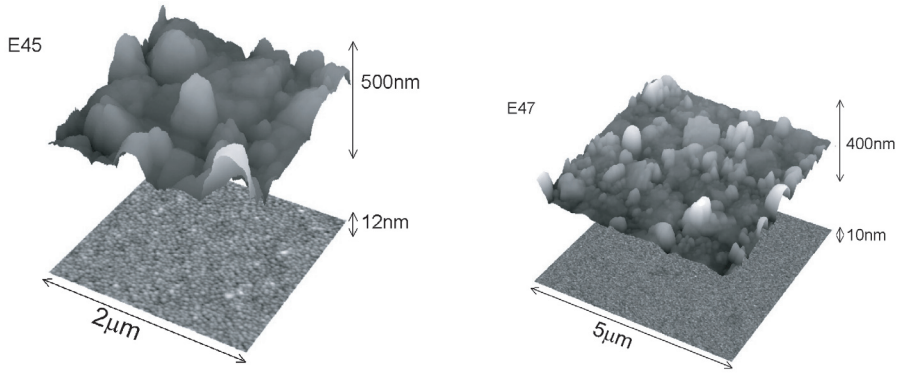

Fig. 3. Comparison between the surface morphology of the buffered substrate and the YBCO film for (a) sample E45 (lower Si/YSZ/CeO_2, upper YBCO) and (b) sample E47 (lower Si/YSZ, upper YBCO).

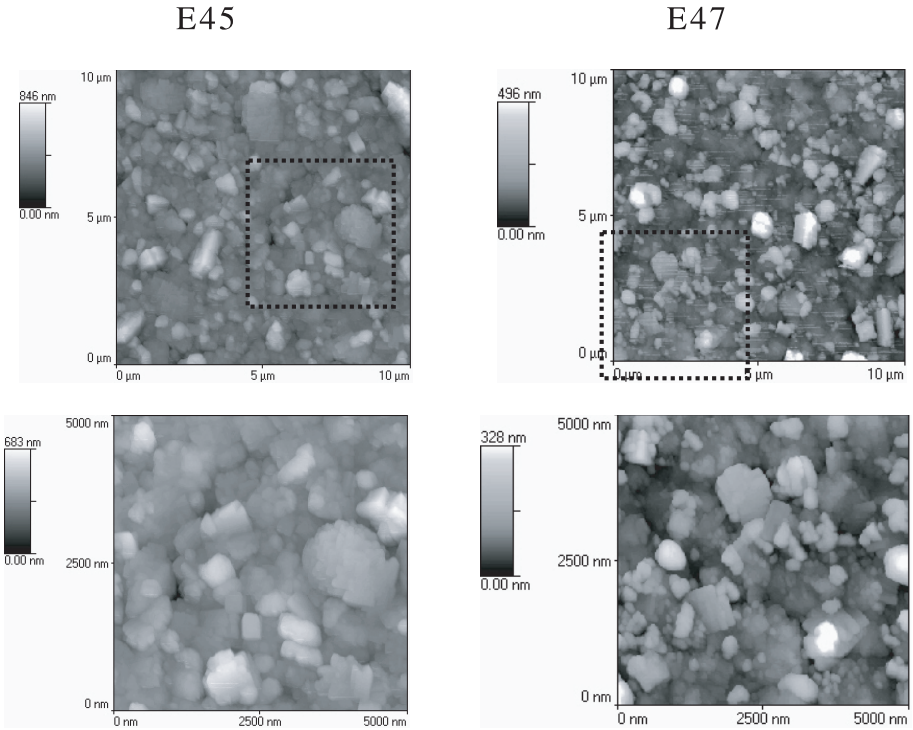

Fig. 4. Non-contact AFM images of samples E45 and E47. The surface of each sample is shown at two different enlargements; the dashed squares in the 10 μm $\times$ 10 μm images indicate the zone reported in the corresponding 5 μm $\times$ 5 μm enlargements.

Figure 4. Both the samples result to be granular, although sample E47 exhibits a more compact structure with a reduced amount of surface holes. A lower number of high-angle grain-boundaries is also hinted by the comparative analysis reported in Figure 5 of the 10 μm $\times$ 10 μm images of Figure 4.

4 Transport characterization

In Figure 6a ρ vs. T measurements are plotted for both the samples at different bias currents. Samples E45 and E47 show transition temperatures $T_c = 87.31$ K and $T_c = 85.70$ K, respectively. The transition width, evaluated by means of the full width at half maximum (FWHM) of the first R vs. T derivatives (Fig. 6b), result to be 5.9 K for sample E45 and 9.0 K for sample E47.

In order to investigate the current transport mechanism, electric field vs. current density ($E-J$) characteristics were performed in the range of temperatures between 18 and 30 K (Fig. 7). It turns out that in the transition between the non-dissipative and the flux-flow regimes, E-J curves exhibit a step-like behaviour.

In the flux-flow regime, i.e. for $J > J_c$ (J_c evaluated by the $E = 1$ μV/cm criterion), weak-links behaviour and percolative transport mechanism show up. By analysing the corresponding E-J curves of both samples in the framework of a percolation model [13], we find the expected power law, i.e., $E^{1/k}$ vs. J curves scaling behaviour (Fig. 8). The parameter k can be best evaluated by means

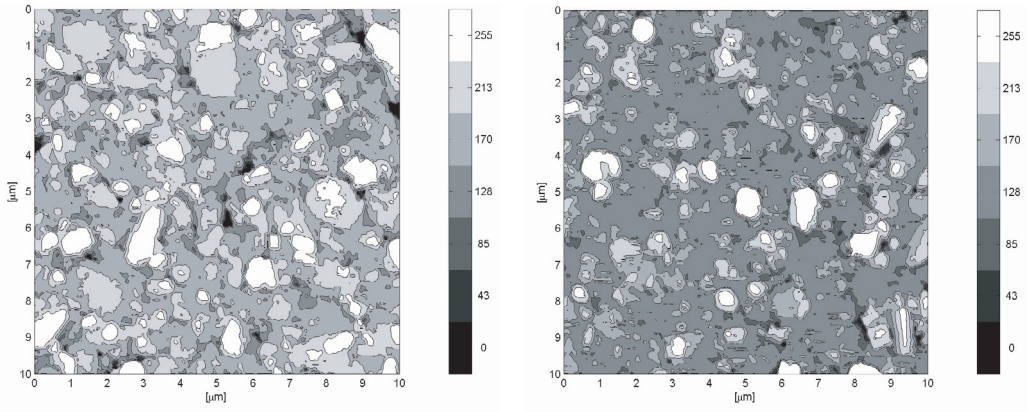

Fig. 5. Filled contour plots of the 10 μm $\times$ 10 μm AFM images of Figure 4 of samples E45 (left) and E47 (right). Different gray tones indicate zones at different depths (arbitrary units). E47 shows a more compact structure pointing also towards a lower number of high-angle grain-boundaries.

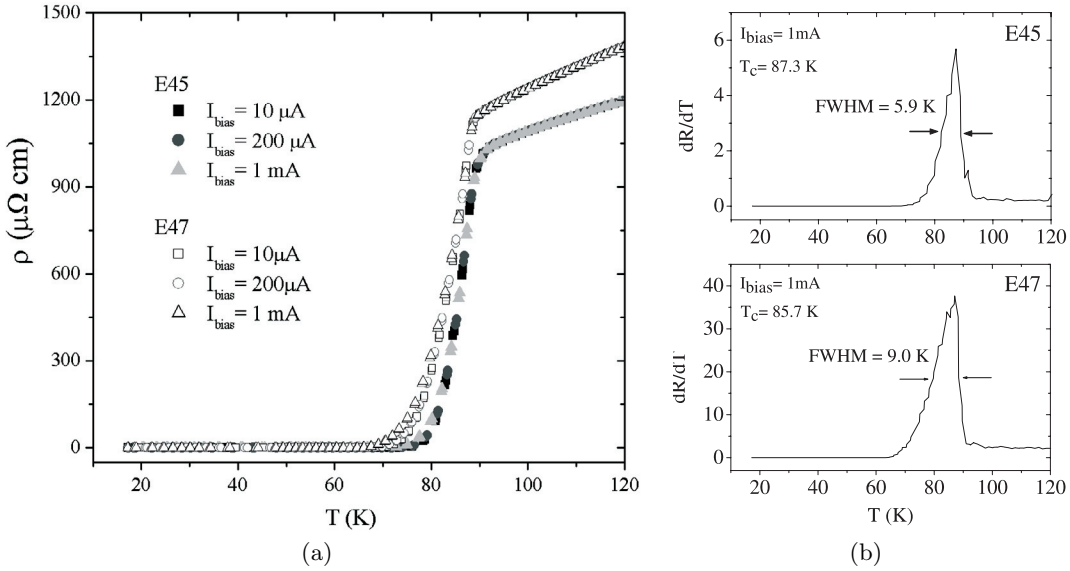

Fig. 6. Temperature dependence of the resistivity, ρ, at different bias currents (a) and first derivative of the R vs. T curves at $I = 1$ mA (b).

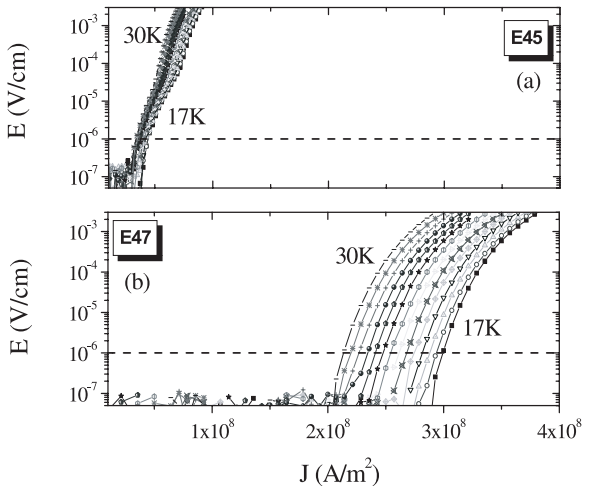

Fig. 7. Electric field vs. current density curves of samples E45 (a) and E47 (b) plotted at different temperatures. Dashed line indicates the electric field threshold 10^{-6} V/cm chosen for the critical current density definition.

of the logarithmic derivative of the E-J curves. The experimental curves $\mathrm{d}(\ln E)/\mathrm{d}(\ln J)$vs. J/J_c of sample E47 are plotted at different temperatures in the inset of Figure 8b and fitted with the law:

$$d(\ln E)/d(\ln J) = k/(1 - J_c/J) \quad J > J_c. \qquad (1)$$

The parameter k turns out to be in agreement with the values reported in [13].

Two different slopes (Fig. 8a) in the $E^{1/k}$ vs. J curves of E45 sample are exhibited. The kink can be attributed to different critical current densities in different areas of the samples [14], likely due to different distribution of grain boundary density and misorientation angles.

It is remarkable that the above mentioned characteristics are accompanied by the presence of linear intrinsic pinning at $J \leq J_c$, as it emerges by the study of the critical current density dependence on temperature. In fact, the J_c vs. T curves result to follow the law predicted for a pinning mechanism accounting for an as-grown linear

defect distribution (Fig. 9) [15]

$$J_c(T) \propto \frac{1}{(\lambda^2(T)\,\xi^{\nu}(T))} \qquad (2)$$

where λ and ξ are the penetration and coherent lengths, respectively, and ν is a fit parameter. According to [15], we have taken $\lambda(T) = \lambda(0)\,(1-t^4)^{-1/2}$ and $\xi(T) = \xi(0)\,[(1+t^2)/(1-t^2)]^{1/2}$ with $t = T/T_c$. The ν parameter, which provides an indication of the defect average diameter, is 1.6 for sample E45 and 2.1 for the sample E47. Therefore, taking into account that the ν value increases as the defect cross-section decreases, it results that the linear defects responsible of the pinning mechanism in sample E47 should be, on average, smaller than those of sample E45, as could be inferred from the AFM surface measurements. These characterizations hint, indeed, to a smaller and more compact crystalline structure with better intergrain coupling in sample E47.

The high temperature crossover of the two J_c vs. T curves for samples E45 and E47 (Fig. 9) confirms the stronger contribution, for sample E47, of linear pinning centres having smaller cross-sections [15]. Such defects are indeed expected to be more effective in a lower range of temperature. Finally, for all the samples, the pinning energy turns out to be in the range of energies calculated by Balents et al. [16] in the case of dislocation lines extending along the entire film thickness [8]. For instance, the calculated pinning energy for sample E47 is 50 meV at 30 K, where the sample exhibits a critical current $J_c = 2 \times 10^8$ A/m^2.

5 Discussion and conclusions

In the framework of the YBCO/Si integration we grew, by means of the magnetron sputtering technique, and fully characterized several Si/YSZ/CeO_2/YBCO typical large-area multilayers. The preparation parameters were optimized in order to grow robust YBCO films with prevailing c-axis orientation. The in-situ growth of CeO_2/YBCO bilayer provided better performance with respect to the preparation where YBCO was grown ex-situ on the Si/YSZ/CeO_2 substrate. In the range of 18–30 K, E vs. J curves exhibit a step-like behaviour. On the other hand, clear signatures of weak-link regime and current percolation show up in the flux flow regime. The percolative nature of the transport current is related to weak-link behaviour among in-plane misoriented grain-boundaries. Grain-boundaries form indeed a corresponding natural network for preferential motion of vortices through the superconductors. At $J \leq J_c$, linear pinning behaviour, pointing to a dynamics driven by weakly pinned vortices in easy flow channels, rather than stronger pinned vortices in the grains, is exhibited.

The linear pinning exhibited by our samples at $J \leq J_c$, accompanied by the percolative behaviour above the critical condition and the relatively low J_c (hinting Josephson junction-like network in the flux-flow region) points

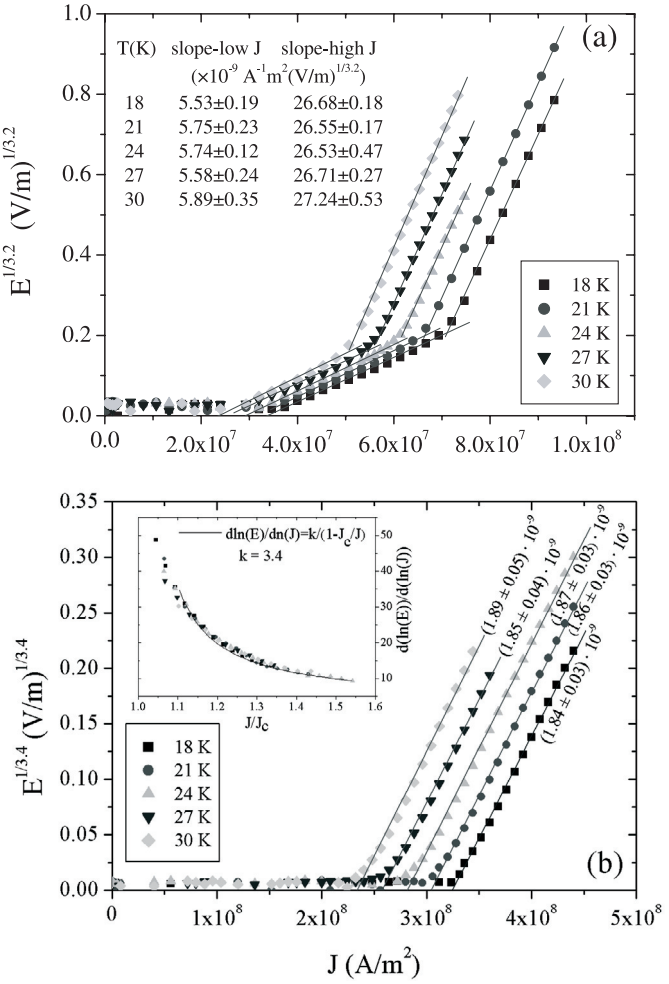

Fig. 8. Electric field vs. current density curves of samples E45 (a) and E47 (b) plotted at different temperatures as $E^{1/k}$ vs. J, with $k = 3.2$ (a) and 3.4 (b). Data are linearly fitted and the slopes are reported in the figures. In the inset of (b) the logarithmic derivatives $\mathrm{d}(\ln E)/\mathrm{d}(\ln J)$ of the curves reported in the main panel are shown and fitted with equation (1) (see text).

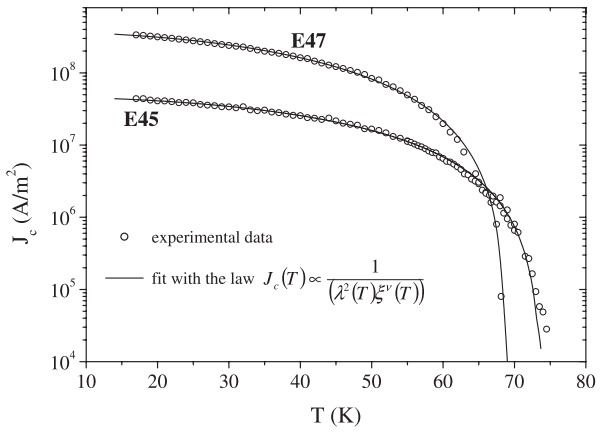

Fig. 9. Critical current density dependence on temperature (symbols) evaluated for both the samples under study. Lines are best fitting curves of the experimental data with equation (2), predicted for pinning by linear defects [13].

to high and fast voltage signal response to external perturbations, respectively. Thus, YBCO thin film microbridges could be exploited for applications such as ultra fast switches [1,17]. The temperature range between 18 and 30 K is an acceptable working region, either with near-I_c bias current [1] or much lower than this limit [17]. The I_c values of our samples for standard strip in the mentioned temperature range are indeed commensurate to the target because the application requires currents not exceeding the capabilities of standard current pulse generators (below 100 mA). The low power consumption, accompanied by a very fast response due to intrinsic nonlocality of the superconducting state, could become the premise of a factory-scalable effective semiconductor-superconductor integration. The development of engineered YBCO/silicon integrated prototypes with suitable read-outs are in progress.

Work partially supported by MIUR under the project FIRB-RBAU01PYB3.

References

1. A. Jukna, R. Sobolewski, Supercond. Sci. Tecnhol. **16**, 911 (2003)
2. G. Beddies, B. Leibold, H.-U. Habermaier, G. Lu, Physica C **185–189** 2101 (1991)
3. L. Méchin, G. Huot, D. Bloyet, Appl. Phys. Lett. **85**, 3154 (2004), and references therein
4. L. Méchin, J.C. Villegier, G. Rolland, F. Laugier, Physica C **269**, 124 (1996)
5. J.M. Phillips, J. Appl. Phys. **79**, 1829 (1996)
6. T. Ami, Y. Ishida, N. Nagasawa, A. Machida, M. Suzuki, Appl. Phys. Lett. **78**, 1361 (2001)
7. A. Chiodoni, V. Ballarini, D. Botta, C. Camerlingo, F. Fabbri, S. Ferrari, R. Gerbaldo, G. Ghigo, L. Gozzelino, F. Laviano, B. Minetti, C.F. Pirri, G. Tallarida, E. Tresso, E. Mezzetti, Appl. Surf. Sci. **238**, 485 (2004)
8. A. Chiodoni, C. Camerlingo, R. Gerbaldo, L. Gozzelino, F. Laviano, B. Minetti, C.F. Pirri, G. Rombolà, G. Tallarida, E. Tresso, E. Mezzetti, IEEE Transactions on Applied Superconductivity **15**, 3062 (2005)
9. F. Laviano, D. Botta, A. Chiodoni, R. Gerbaldo, G. Ghigo, L. Gozzelino, E. Mezzetti, Phys. Rev. B **68**, 014507 (2003)
10. J. Qiao, C.Y. Yang, Mat. Sci. Eng, **R14**, 157 (1995)
11. B.D. Cullity, *Elements of X-ray diffraction* (New York, USA, Addison-Wesley, 1998)
12. H.Y. Zhai, Z.H. Zhang, W.K. Chu, Appl. Phys. Lett. **78**, 649 (2001)
13. B. Zeimetz, B.A. Glowacki, J.E. Evetts, Eur. Phys. J. B **29**, 359 (2002)
14. B. Zeimetz, B.A. Glowacki, J.E. Evetts, Physica C **372**, 767 (2002)
15. F.C. Klassen, G. Doornbos, J.M. Huijbregtse, R.C.F. van der Geest, B. Dam, R. Greissen, Phys. Rev. B **64**, 184523 (2001)
16. L. Balents, M. Kardar, Phys. Rev. B **49**, 13030 (1994)
17. A.D. Semenov, G.N. Gol'tsman, R. Sobolewski, Supercond. Sci. Technol. **15**, R1 (2002)